ACS APPLIED MATERIALS & INTERFACES

Research Article

www.acsami.org

Thermal Conductivity of Freestanding Single Wall Carbon Nanotube Sheet by Raman Spectroscopy

Satyaprakash Sahoo,*[,†] Venkateswara Rao Chitturi,[†] Radhe Agarwal,[†] Jin-Wu Jiang,[‡] and Ram S. Katiyar*[,†]

[†]Department of Physics and Institute for Functional Nanomaterials, University of Puerto Rico, San Juan, Puerto Rico 00931, United States

[‡]Shanghai Institute of Applied Mathematics and Mechanics, Shanghai Key Laboratory of Mechanics in Energy Engineering, Shanghai University, Shanghai 200072, People's Republic of China

Supporting Information

ABSTRACT: Thermal properties of single wall carbon nanotube sheets (SWCNT-sheets) are of significant importance in the area of thermal management, as an isolated SWCNT possesses high thermal conductivity of the value about 3000 W m^{-1} K^{-1}. Here we report an indirect method of estimating the thermal conductivity of a nanometer thick suspended SWCNT-sheet by employing the Raman scattering technique. Tube diameter size is examined by the transmissions electron microscopy study. The Raman analysis of the radial breathing modes predicts narrow diameter size distribution with achiral (armchair) symmetry of the constituent SWCNTs. From the first order temperature coefficient of the A_{1g} mode of the G band along with the laser power dependent frequency shifting of this mode, the thermal conductivity of the suspended SWCNT-sheet is estimated to be about ~18.3 W m^{-1} K^{-1}. Our theoretical study shows that the thermal conductivity of the SWCNT-sheet has contributions simultaneously from the intratube and intertube thermal transport. The intertube thermal conductivity (with contributions from the van der Waals interaction) is merely around 0.7 W m^{-1} K^{-1}, which is three orders smaller than the intratube thermal conductivity, leading to an abrupt decrease in the thermal conductivity of the SWCNT-sheet as compared to the reported value for isolated SWCNT.

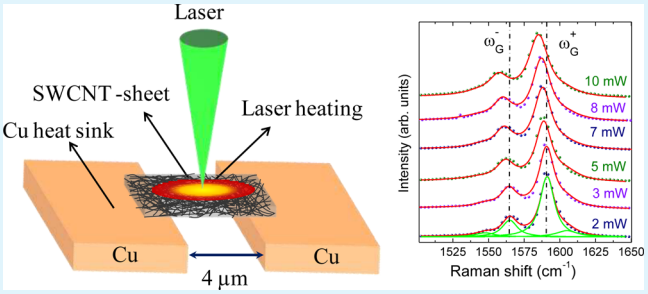

KEYWORDS: *single wall carbon nanotube, Raman spectroscopy, phonon, thermal conductivity, chemical vapor deposition, MD simulation*

INTRODUCTION

Carbon nanotubes (CNTs) are an allotrope of carbon, in which carbon atoms are bonded each other to form tiny cylinders.[1−4] Among CNTs, single walled carbon nanotubes (SWCNTs) are of great research interest due to their extraordinary physical properties such as higher thermal conductivity and ballistic electron transport.[5−9] Individual SWCNTs can have very high thermal conductivity (as high as 3000 W m^{-1} K^{-1} or even higher as predicted theoretically);[10−12] thus, SWCNTs are a very promising material for thermal management applications. However, for practical applications, especially for thermal management, SWCNT-sheets are often desired. In the literature, there are wide discrepancies in the thermal conductivity values for various CNT systems, i.e., from individual isolated CNTs to their assembly (thread, sheet, etc.).[13−16] In most of the earlier reports, SWCNT-sheets have either broader diameter size distribution or embedded in a polymer matrix.[17,18] Thus, the intrinsic thermal conductivity has not been realized. In view of this, it is necessary to shed light on the thermal property of defect free, narrow diameter size distributed, and suspended SWCNT-sheet. The heat energy in solids is transferred by the quantized lattice vibration called phonons and free electrons. Both of these contribute to the intrinsic thermal conductivity of solids.[19] In metals the thermal conductivity has contributions predominantly from free electrons, whereas in semiconductors and insulators, phonon contribution dominates. As Raman spectroscopy probes the zone center phonons and phonon related phenomena in solids,[20−24] it could possibly be used as a potential tool to estimate the lattice thermal conductivity of carbon materials.

Herein, we report an indirect method for estimating the thermal conductivity of a nanometer thick suspended SWCNT-sheet by employing the Raman scattering technique. The tube diameter of our sample is confirmed by the transmission electron microscopy and Raman scattering studies. Thermal conductivity of the suspended SWCNT-sheet has been

Received: August 14, 2014
Accepted: October 28, 2014
Published: October 28, 2014

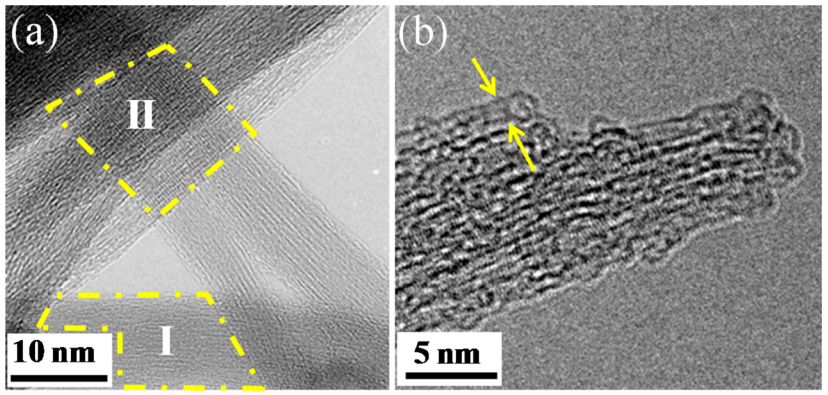

Figure 1. (a) TEM image of the SWCNT-sheet. The image is obtained from one of its edges. Regions I and II show the aligned and unaligned tube domains of the sheet, respectively. (b) A typical image with higher magnification, that shows a narrow diameter size distribution of the tube.

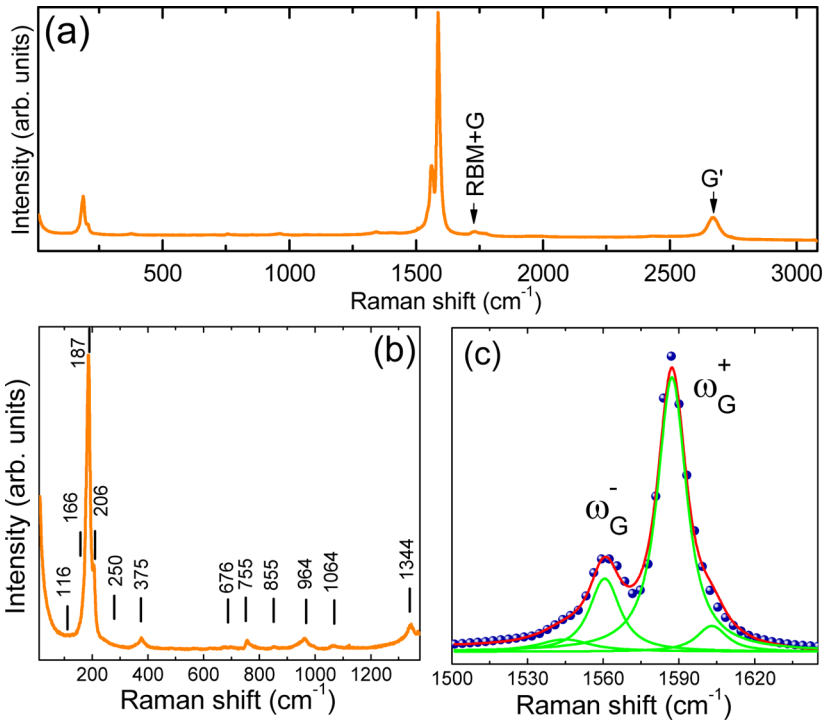

Figure 2. (a) Room temperature Raman spectra of SWCNT-sheet. (b) Portion of part a shows clear low intense peaks. (c) The G band is fitted with four peaks.

estimated from first order temperature coefficient of the A_{1g} mode of G band, along with laser power dependent frequency shifting of this mode. Our experimental finding of the low thermal conductivity is explained by our theoretical calculation.

EXPERIMENTAL SECTION

Thermal chemical vapor deposition technique was used for the growth of high quality SWCNTs. In a typical procedure,[25] 100 mg of Fe/MgO (0.6 wt % Fe) catalyst was uniformly spread in the quartz boat, and the quartz boat was placed in the middle of quartz tube (inner diameter 22 mm) mounted in a temperature-controlled cylindrical horizontal furnace. The furnace was heated up to 1023 K, with the Ar gas flow, and then, high purity grade methane/argon (20:80) was introduced for 10 min at a flow rate of 750 cc/min. The furnace was then cooled to room temperature under Ar atmosphere. In order to remove the Fe- and Mg-based impurities (Fe, FeO_x, and MgO_x) and amorphous carbon from the as-grown SWCNTs, the material is purified in three-step process which minimizes the damage to the SWCNTs. In the first step, the dense sheet of composite powder (500 mg) was sonicated with 50 mL of concentrated HCl (37% HCl in H_2O) at room temperature, to extract the SWCNTs by dissolution of MgO_x, FeO_x and Fe impurities present in the sample. The resultant product was washed with deionized water until neutrality, washed with methanol, filtered, and dried under vacuum for 8 h at 60 °C. In the second step, 300 mg of HCl-treated SWCNTs was dispersed in 100 mL of 6 M HNO_3 in a round-bottom flask, refluxed at 70 °C for 24 h to remove Fe particles as well as amorphous carbon, and then washed with water/methanol, filtered, and dried at 80 °C in a vacuum oven for 12 h. In the last step, dried SWCNT powder was heat-treated at 300 °C for 1 h under Ar atmosphere. Raman measurements were carried out using a Horiba-Jobin T64000 micro-Raman system, and a diode laser with excitation wavelength of 514.5 nm was used. The temperature dependent Raman studies are carried out by changing the sample temperature by an external temperature controller. These samples are characterized using a high resolution transmission electron microscopy (HRTEM, JEOL JEM-2200FS). The thermal transport is simulated by the direct MD simulation method implemented in the LAMMPS package.[26] The C−C interactions in the SWCNT crystalline sample were described by the Adaptive Intermolecular Reactive Empirical

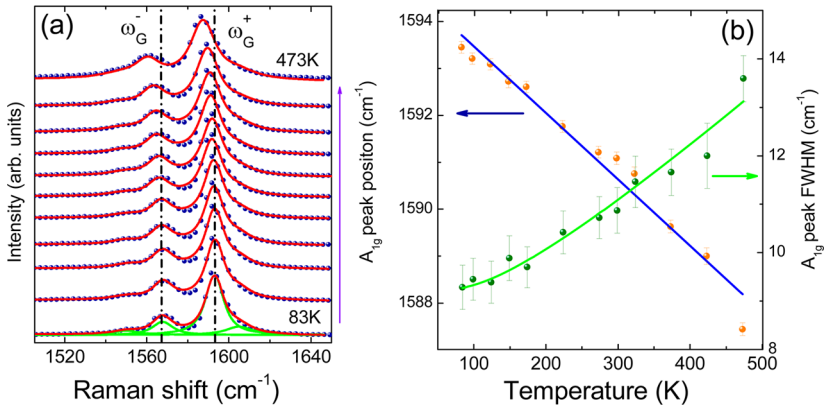

Figure 3. (a) Temperature dependent Raman spectra of the G band of SWCNT-sheet. (b) Plot of peak position and fwhm of the A_{1g} peak, with the solid lines being the fitting to the data.

Bond Order (AIREBO) potential.[27] The distance cutoff for the Lennard-Jones potential in the AIREBO was chosen as 1.02 nm. The thermal current across the system is driven by frequently moving kinetic energy from the cold region to the hot region.[28] This energy transfer is accomplished via scaling the velocity of atoms in the hot or cold temperature-controlled regions. The total thermal current pumped into the hot region (or pumped out from the cold region) is $J = \alpha E_k^{\text{hot}}$. We have introduced a current parameter α to measure the energy amount to be aggregated per unit time. We note that the total current J is the *eflux* parameter in the *fix heat* command in LAMMPS. The physical meaning of the parameter α is the ratio between the aggregated energy and the kinetic energy of each atom; i.e., α measures the thermal current for each atom with respect to its kinetic energy.[29] The velocity scaling operation was performed every τ ps, which can be regarded as the relaxation time of this particular heat bath. We chose τ = 0.04 ps in all simulations.

RESULTS AND DISCUSSION

Figure 1a shows a typical high resolution transmission electron microscopy image of purified CNT. In the figure, we have highlighted two regions, I and II; these clearly show that the CNT-sheet consists of both aligned and unaligned tube domains with large packing density. A higher magnification image is shown in Figure 1b, and it can be seen from the figure that our CNT sample consists of SWCNTs. Further analysis of these images reveals a narrow tube diameter distribution.

Figure 2a shows the room temperature Raman spectra of our CNT sample recorded over a wide wavenumber range (10−3200 cm^{-1}). For comparison we have provided Raman spectra of as-synthesized (bottom) and purified (top) SWCNT-sheet (see Supporting Information Figure S1).

Distinct peaks can be noticed in the low ($\omega \leq 500$ cm^{-1}), mid ($500 \leq \omega \leq 1800$ cm^{-1}), and high ($1800 \leq \omega \leq 3200$ cm^{-1}) frequency regions of the spectra. The observed Raman spectra resemble those from previous reports of SWCNTs.[30−32] In other allotropes of carbon, such as graphite and graphene, Raman modes at the low frequency side are absent (expect for the shear mode in graphite at 30 cm^{-1});[33] however, due to confined geometry of CNTs, Raman selection rules impose some of the modes in the low frequency region.[34] These Raman active modes have either $E_{1/2g}$ or A_{1g} symmetry which originates from the coherent vibration of the carbon atoms in the radial direction tube. These are called radial breathing modes (RBMs). Its peak frequency is tube diameter dependent (frequency is inversely proportional to the diameter for a homogeneous cylindrical tube) and hence useful in estimating the tube diameter precisely. In order to provide a clear picture of these RBM modes along with other low intensity peaks, we have plotted the spectra from 10 to 1370 cm^{-1} separately in Figure 1b, and peak positions are indexed.

The various properties of SWCNTs depend on the manner in which a graphene sheet is rolled up to form SWCNTs, and the latter is determined by the chiral index (n_1, n_2).[35] a SWCNT with unequal, nonzero values of chiral index has chiral symmetry. For achiral SWCNTs, those with chiral index of (n_1, 0) and (n_1, n_1) are called *zigzag* and *armchair*, respectively.[36] Several theoretical calculations have been reported on the possible number of Raman modes and their frequencies by considering different chiral indexes. Our observed Raman modes and their frequencies match well for sets of armchair tubes with indexes (8, 8), (9, 9), (10, 10), and (11,11).[37] Note that it has been theoretically predicted that these are the most stable armchair SWCNTs. The geometrical diameter of the tube in terms of the chiral index can be expressed as $d = a_0(n_1^2 + n_1n_2 + n_2^2)^{1/2}/\pi$ where a_0 is the in-plane lattice constant of graphite (a_0 = 2.441 Å). For armchair SWCNTs where $n_1 = n_2$, the tube diameter linearly depends on n_1 as $d = 1.356n_1$. The estimated diameters of SWCNTs with chiral indexes of (8,8), (9,9), (10,10), and (11,11) are 1.08, 1.2, 1.35, and 1.49 nm, respectively. These sets of tube diameters are consistent with the TEM results (see TEM histogram in the Supporting Information Figure S2). It may be pointed out that although the Raman spectra indicate the majority of nanotubes have *armchair* chiral symmetries, however, the presence of nanotubes with chiral symmetry cannot be ignored in the sample.

An intense peak can be observed in the midfrequency range of Raman spectra (1500−1600 cm^{-1} frequency range), which is known as the G band.[38] Unlike graphite and graphene, the G band of SWCNT arises due to the zone folding of the graphene. Brillouin zone and the G band (*armchair*) is a triplet with Raman active A_{1g}, E_{1g}, and E_{2g} symmetries. The Raman spectra of the G band is best fitted using a theoretically obtained Raman line shape (damped harmonic oscillator model) which can be written as[39]

$$I(\omega) = \frac{\chi_0 \Gamma_0 \omega \omega_0^2 (\bar{n} + 1)}{(\omega_0^2 - \omega^2)^2 + \omega^2 \Gamma_0^2} \quad (1)$$

Here, $n = \exp((-\hbar\omega)/(k_B T)) - 1$ is the phonon occupation number, ω_o and Γ_0 are the peak position and the line width, respectively, and χ_o is related with peak intensity. The G band is best fitted by four peaks (see Figure 1c) at about 1547.2, 1565, 1592, and 2006 cm^{-1}, and these peaks are identified as E_{2g},

dx.doi.org/10.1021/am505484z | ACS Appl. Mater. Interfaces 2014, 6, 19958−19965

(A_{1g},E_{1g}), A_{1g}, and E_{2g}, respectively, on the basis of the previously reported polarized Raman studies.[40] The low (ω_G^-) and high (ω_G^+) frequency side of the G band is associated with vibration of carbon atoms along the circumferential and the nanotube axis direction, respectively. It has been verified both theoretically and experimentally that the A_{1g} mode appearing at 1592 cm^{-1} is the most intense peak in armchair SWCNTs. Now we will consider this mode for further analysis of our results.[41] It may be noted that the D (1344 cm^{-1}) peak intensity in a carbon material is the measure of defect concentration in carbon material. The D peak intensity is about 100 times lower than that of G peak indicating good quality of our sample. In the Raman spectra, some of the weak peaks originate from two phonon scattering processes (combinational or second order phonon).

As mentioned in the Introduction, the central idea behind this work is to estimate the thermal conductivity of SWCNT-sheet with low defects and narrow diameter size distribution. In order to estimate the thermal conductivity, we will follow similar procedure as in our recent report for few layer MoS_2 and other published reports.[42,43] For this we will first focus on the temperature dependent Raman study of SWCNTs. Figure 3a shows the Raman spectra of the G band of the sample recorded over a temperature window 83−473 K. It can be seen from the figure that with increase in temperature the G band shows a systematic red-shift. Moreover, a noticeable broadening of the G band is observed with increase in temperature. These spectra are further analyzed by fitting four peaks as discussed above, and the intense peak at 1592 cm^{-1} (A_{1g}) is chosen for the temperature dependency study. The plot of the peak position of this peak versus temperature is shown in Figure 3b. The temperature dependence of this peak position follows a linear behavior, and the data is best fitted by considering the following linear equation $\omega = \omega_0 + \alpha T$, where ω_0 is the frequency at 0 K, and α is the first order temperature coefficient. The value of first order temperature coefficient (α) is found to be -1.7×10^{-2} cm^{-1} K^{-1}. The obtained value closely matches with that of graphene.[44] The red-shift of the optical phonon with increase in temperature is generally associated with a combinational effect of volume contribution (thermal expansion) and temperature contribution, resulting from anharmonicity in the crystal lattice. The phonon frequency can be expressed in terms of volume and temperature as:[45]

$$\left(\frac{\partial \ln \omega}{\partial T}\right)_P = \left(\frac{\partial \ln V}{\partial T}\right)_P \left(\frac{\partial \ln \omega}{\partial \ln V}\right)_T + \left(\frac{\partial \ln \omega}{\partial T}\right)_V = -\frac{\gamma}{k}\left(\frac{\partial \ln \omega}{\partial P}\right)_T + \left(\frac{\partial \ln \omega}{\partial T}\right)_V \quad (2)$$

Here $\gamma \sim (\partial \ln V/\partial T)_P$ and $k \sim -(\partial \ln V/\partial P)_T$ are the volume thermal coefficient and isothermal volume compressibility, respectively.

Now, we will discuss the temperature dependent broadening of peak at 1592 cm^{-1} (A_{1g}). The fwhm of this mode as a function of temperature is plotted in Figure 3b. If the lattice crystal were a perfect harmonic crystal, one would have expected an infinitesimal Raman line width. In reality, anharmonicity existing in the lattice forces allows optical phonons to interchange their vibrational energies to other phonon modes. In that case, an optical phonon can decay into either two acoustic phonons of equal and opposite momentum (Klemens channel) or one optical and one acoustic phonon (Ridley channel).[46] We will now focus on a qualitative description of the temperature dependency of the first order Raman scattering by considering the generalized decay channel. If we consider the contribution to line width that arises from the decay of zone center optical phonon into one acoustic and one optical phonon, then it may be possible to express the temperature dependent phonon line width as[47]

$$\Gamma(T) = \Gamma_0 + A[1 + n(\omega_1, T) + n(\omega_2, T)] \quad (2)$$

where Γ_0 is the background contribution, A is the anharmonic coefficient, and $n(\omega, T)$ is the Bose−Einstein distribution function. The values of Γ_0, A, ω_1, and ω_2 used in the above equation are 4.5, 2, 250, 1340 cm^{-1}, respectively, and the fitted line to the data is shown in Figure 3b. It may be further noted that the anharmonic process that accounts for multiphonon recombination is not the only cause of Raman line shape. Additional broadening of the G^+ was observed in SWCNT bundles due to the tube−tube interaction.[48] Defects and isotopes can affect the Raman line shape by disturbing the translation symmetry of crystal. However, the presence of poor D band intensity ruled out defect contribution to the broadening.

As a second procedure to evaluate the thermal conductivity of SWCNTs, it is necessary to study the dispersion of 1592 cm^{-1} (A_{1g}) mode over change in laser power on a free-standing SWCNT-sheet. In this case, the heat conduction to the sink is purely through SWCNT-sheet. The choice of freestanding sample is desired as heat generated from laser power will be dissipated to the substrate, and it would result in inappropriate information about the change in the peak frequency over laser power. A suspended freestanding SWCNT-sheet is fabricated by suspending the sample on a TEM grid (with no carbon support) as shown in Figure 4a. As Cu has high thermal

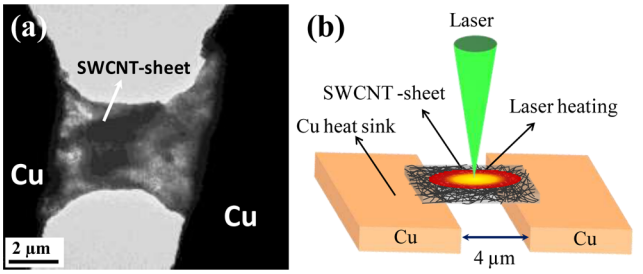

Figure 4. (a) TEM image of the suspended SWCNT-sheet. (b) Schematic representation of the SWCNT-sheet with laser heating.

conductivity (~390 W m^{-1} K^{-1}), it will serve as heat sink.[49] Hence, it is assumed that increase in laser power will not affect the temperatures of the heat sink. The suspended SWCNT-sheet nearly resembles a rectangular geometry where two edges are supported on the copper grid. The length and the width of the suspended sheet are about 4 and 3 μm, respectively. Our laser spot size is about 1.5 μm, and in order to ensure uniform/homogeneous heat energy propagation to the copper (heat sink), the laser was focused at the center of the suspended sheet. The schematic representation of laser heating on the suspended SWCNT-sheet is shown in Figure 4b.

For steady and uniform heat conduction through a plane laminar surface of area A, the heat flow can be expressed by the conventional heat flow equation as $((\partial Q)/(\partial t)) = -k \oint \nabla T \, dA$, where k is the thermal conductivity and T is the absolute temperature. The term at the left-hand side of the equation

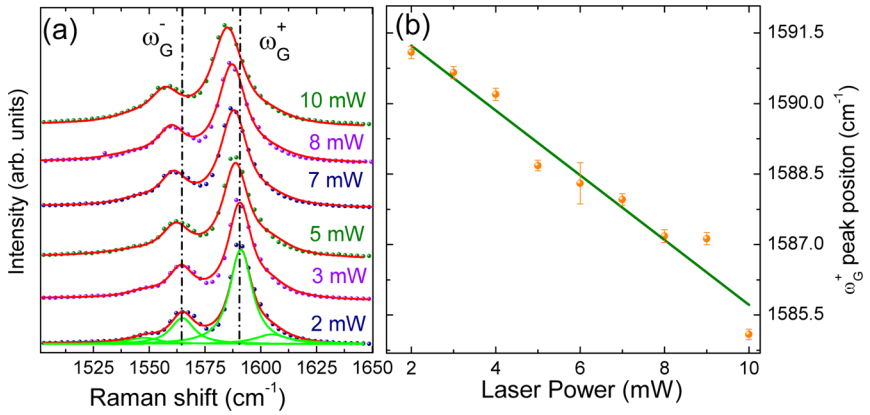

Figure 5. (a) Laser power dependent Raman spectra of the G band of suspended SWCNT-sheet. (b) Plot of A_{1g} peak positions with laser power. The solid line is the fitting to the data.

represents the heat flux. In a recent study Balandin et al.[50] have modified the above equation while estimating the thermal conductivity of a suspended monolayer graphene using Raman spectroscopy. The modified equation in term of thickness and incident laser power is given by $k = (1/2\pi h)(\Delta P/\Delta T)$ where h is the thickness of the layer, and ΔP is the difference in laser power. By recalling the linear equation that we have used previously to fit the temperature dependency of A_{1g} mode and differentiating it with respect to power, the expression for the thermal conductivity can now be written as follows:

$$k = \chi_{A1g}\left(\frac{1}{2\pi h}\right)\left(\frac{\delta\omega}{\delta P}\right)^{-1} \tag{3}$$

Here, χ_{A1g} and $\delta\omega/\delta P$ are the first order temperature coefficient and the change in frequency with incident laser power of A_{1g} mode, respectively.

We change the laser power from 2 to 10 mW, and for each power the Raman spectra of the suspended SWCNT-sheet was recorded which is shown in Figure 5a. These spectra were fitted with four peaks using a damped harmonic oscillator model as discussed previously. The G mode (both ω_G^- and ω_G^+ components) has undergone monotonous red-shifting and broadening with increase in laser power. The above changes in the Raman line shape suggest that the increase in laser power has significantly increased the local temperature. Using the peak position, the local temperature is extrapolated from the temperature dependent peak position relation. The local temperature due to 10 mW laser power is estimated to be about 750 K. The laser power dependent peak position of the intense A_{1g} mode is plotted in Figure 5b. As the frequency changes linearly with laser power, we fitted the data with a straight line, and the slope of that line gives us the value of the $\delta\omega/\delta P$, i.e., rate of change of the A_{1g} mode frequency with laser power. The average value of $\delta\omega/\delta P$ is found to be about 0.73 cm^{-1}/mW.

The only parameter in eq 3 which has to be determined is thickness of the SWCNT-sheet. We employed electron energy loss spectroscopy (EELS) to estimate the thickness. Thickness measurement in terms of the inelastic mean free path (MFP) can be useful for measuring the relative thicknesses of similar specimens or thickness variations within a specimen of uniform composition. Thickness is related to the effective mass (Z_{eff}), incident electron energy (E_0), collection angle (β), etc. The thickness t is given by $t/\lambda = \ln(I_t/I_0)$, where λ is the total mean free path for all inelastic scattering and can be calculated by[51]

$$\lambda \approx \frac{106F(E_0/E_m)}{\ln(2\beta E_0/E_m)} \tag{4}$$

Here, F is a relativistic factor (0.768 for E_0 = 100 keV, 0.618 for E_0 = 200 keV). Our calculation and EELS studies for this sample result in $\lambda \approx 117$ and thickness about 170 ± 10 nm.

Using the values of $\delta\omega/\delta P$, first order temperature coefficient of A_{1g} mode ($\chi_{A1g} = -1.43 \times 10^{-2}$ cm^{-1}/K), and thickness of the FLMS (h = 170 nm) in eq 3, the average extracted thermal conductivity of FLMS is found to be ~18.3 W m^{-1} K^{-1}.

The thermal transport in isolated CNT is determined by phonon due to the strong sp^2 bonding and limited by the anharmonicity in the lattice potential. Second, the measured phonon mean free path for CNT is about 700 nm for tube length of 2 μm.[52] Although the mean free path has lower value than the tube length but is still comparable, thermal transport thus approaches the ballistic regime. However, for a randomly oriented CNT-sheet, extrinsic thermal transport, i.e., phonon scattering by boundary or tube junctions, cannot be ignored. Due to the network structure of the sheet, the phonon mean path is expected to reduce significantly resulting in pure diffusive heat transport. This results in lower value of thermal conductivity in SWCNT-sheet. Sten et al.[53] have measured the thermal conductivity of multiwalled CNT bundle using 3-ω method. Their result shows a low thermal conductivity for multiwalled CNTs, and according to them, the low value of thermal conductivity is due to disorder in the material.

Theoretical Results. As mentioned earlier the thermal transport in the isolated CNT is determined by phonon due to the strong sp^2 bonding and is mainly limited by the phonon−phonon scattering in pure samples. The phonon−phonon scattering is so weak for the flexure mode in the isolated CNT that this mode has an extremely long lifetime, resulting in the superior thermal conductivity of the isolated CNT. However, for a randomly orientated CNT-sheet, the intertube thermal transport plays an important role; i.e., heat energy needs to be transferred from a CNT to its neighboring tubes. CNTs in the network structure are connected to each other through the weak van der Waals interaction, which should impose a strong limitation on the thermal transport ability of the CNT-sheet. We thus perform molecular dynamics simulations to illustrate the effect of the van der Waals interaction on the thermal conductivity of the CNT-sheet as follows.

Our theoretical study focuses on the crystalline SWCNT, which can be regarded as a special configuration of the

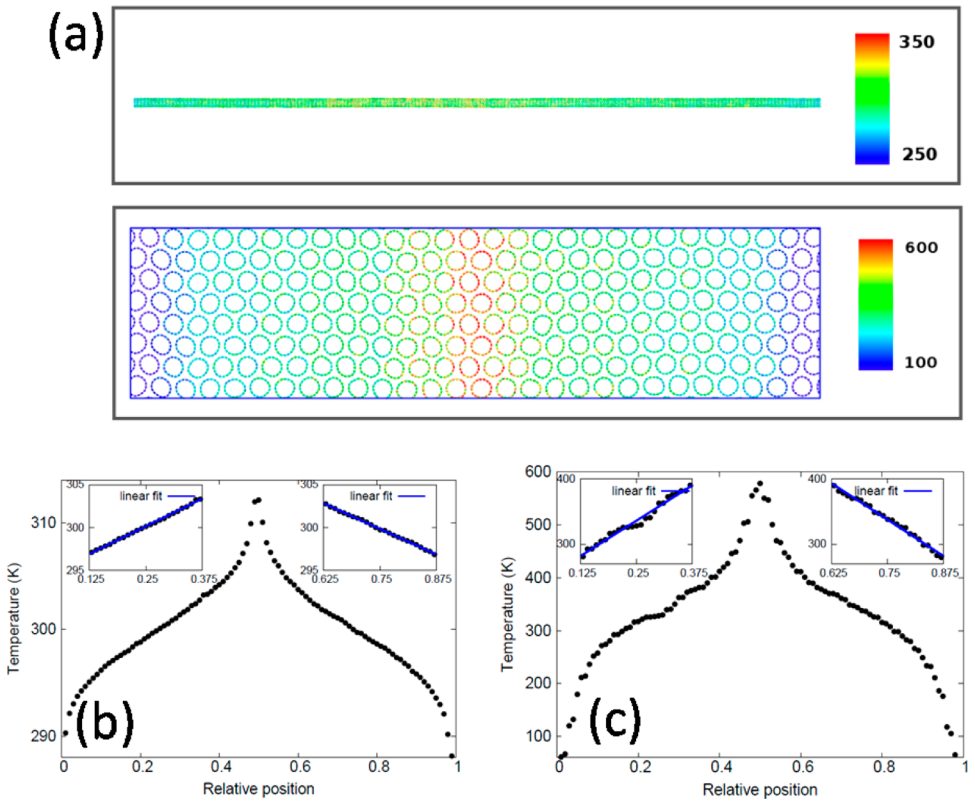

Figure 6. (a) Structure of the crystalline SWCNT. Top: side view for SWCNTs (8, 8). Thermal energy is transported along the tube axis. Bottom: axial view for the crystalline SWCNT. Thermal energy is transport across the SWCNT. Color bar is with respect to the atomic temperature. (b) Temperature profile at 300 K for a SWCNT. The current ratio $\alpha = 0.1$, and the relaxation time of the heat bath is $\tau = 0.04$ ps. The top left inset shows the linear fitting for the profile in $x \in [0.125, 0.375]$, giving a temperature gradient dT/dx_1. The right inset shows the linear fitting for the profile in $x \in [0.625, 0.875]$, giving a temperature gradient dT/dx_2. These two temperature gradients (dT/dx_1 and dT/dx_2) are averaged in the calculation of the thermal conductivity using the Fourier law. (c) Temperature profile at 300 K for the intertube thermal transport of the crystalline SWCNT. Insets show the linear fitting for the left and right parts to extract the temperature gradient.

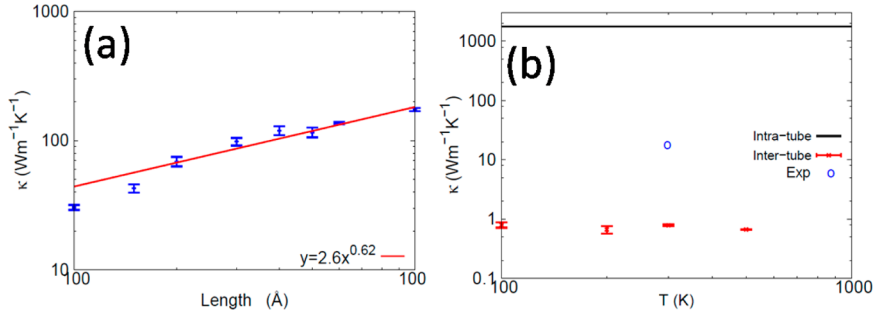

Figure 7. (a) Length dependence of the thermal conductivity for the SWCNT with diameter $d = 1.08$ nm at 300 K. Data are fitted to a power function. (b) The comparison between the intratube and the intertube thermal conductivity. The solid line in the top region is the intratube thermal conductivity at 300 K for a free SWCNT of $L = 4.0$ μm in length, as predicted by the power function $k = 2.6L^{0.62}$ in part a. Red dots are for intertube thermal conductivity of the crystalline SWCNT, where the diameter of the SWCNT is 1.08 nm. Blue circle is the experimental thermal conductivity for SWCNT-sheet, in which the SWCNT is 4.0 μm in length and 1.08 nm in diameter.

SWCNT-sheet. Figure 6a shows the configuration of a SWCNT in the top panel and the SWCNT-sheet in the bottom panel. In the crystalline SWCNT shown in the bottom panel, all armchair SWCNTs (8, 8) are closely aligned and parallel to each other. The diameter of the SWCNT is 1.08 nm that is close to the experiment sample. We study the difference between the intratube and the intertube thermal conductivity. The former describes the heat transport along the tube axis, while the latter captures the ability of delivering heat energy from a SWCNT to its neighboring tubes. Figure 6b shows the temperature profile for a SWCNT at 300 K. The SWCNT is 74.8 nm in length. The two insets show that the left middle region with relative axial position in [0.125, 0.375] and the right middle region within [0.625, 0.875] are linearly fitted to extract two temperature gradients. These two temperature gradients are averaged to give the final temperature gradient dT/dx. The thermal conductivity is obtained through the Fourier law $k = (1/2) \times (J/|(dt/dx)|)$, where a factor of $^1/_2$ comes from the fact that heat current flows in two opposite directions. The difference between the left and right temperature gradients is used to estimate the numerical error in the thermal conductivity.

Figure 6c shows the intertube temperature profile in the crystalline SWCNT at 300 K. Each tube in the crystalline is 1.97 nm in length and 1.08 nm in diameter. The parameter α = 0.01 is chosen to be 1 order smaller than that used in the simulation of the intratube thermal transport. It is because the intertube thermal conductivity is so small that atoms in cold regions will be frozen if their kinetic energies are pumped out too fast.

As the first step, we simulate the thermal transport in a free SWCNT. Figure 7a presents the length dependence of the thermal conductivity for the free SWCNT at 300 K. The thermal conductivity in the free SWCNT does not saturate at a constant value with increasing length, because of the abnormal lifetime of the flexure mode in the low-dimensional materials.[54] Data are fitted to a power function $y = 2.6x^{0.62}$. For a given length L = 4.0 μm, the fitting expression predicts a thermal conductivity of k = 1854.6 W m^{-1} K^{-1}. Our experimental thermal conductivity (18.3 W m^{-1} K^{-1}) is about 2 orders smaller than this value. It indicates that the thermal conductivity value measured in the experiment is not merely the intratube thermal conductivity. Figure 7b compares the intratube thermal conductivity with the intertube thermal conductivity. The solid line in the top region is the intratube thermal conductivity at 300 K for a free SWCNT of 4.0 μm in length, which is predicted by the power function $k = 2.6L^{0.62}$ obtained in Figure 7a. Red dots are for intertube thermal conductivity of the crystalline SWCNT. The intertube thermal conductivity is around 0.7 W m^{-1} K^{-1}, which is at least 3 orders smaller than the intratube thermal conductivity. In the SWCNT-sheet sample, tubes are randomly aligned, so they are not in the ideal packed configuration as the crystalline structure. Hence, the thermal conductivity in the SWCNT-sheet is contributed to simultaneously by the intratube and the intertube thermal transport. As a result, we measured a value of 18.3 W m^{-1} K^{-1}, which is sandwiched between the intratube and intertube thermal conductivity.

Conclusions. To summarize our results, a SWCNT-sheet has been synthesized by CVD method. Raman scattering technique is employed to determine the lattice thermal conductivity of SWCNT-sheet of thickness about 170 nm. The analysis of the radial breathing modes in the Raman spectra of the SWCNT-sheet confirms the narrow diameter size distribution of the tubes with achiral (armchair) symmetry. From the temperature dependent Raman spectra of the A_{1g} mode of the G band, the first order temperature coefficient is found to be 1.7×10^{-2} cm^{-1}/K. By measuring the laser power dependent Raman spectra of SWCNT-sheet along with the first order temperature coefficient of A_{1g} mode, the thermal conductivity of the suspended SWCNT-sheet is estimated to be ~18.3 W m^{-1} K^{-1}. The lower value of the thermal conductivity has also been explained and verified by theoretical calculations. Our theoretical study shows that the thermal conductivity of the SWCNT-sheet has simultaneous contributions from the intratube and intertube thermal transport. The intertube thermal conductivity (contributed by the van der Waals interaction) is merely around 0.7 W m^{-1} K^{-1}, which is 3 orders of magnitude smaller than the intratube thermal conductivity, leading to an abrupt decrease in the thermal conductivity of the SWCNT-sheet as compared to that of reported value for isolated SWCNT.

■ ASSOCIATED CONTENT

Ⓢ Supporting Information

Additional Raman and TEM information. This material is available free of charge via the Internet at http://pubs.acs.org.

■ AUTHOR INFORMATION

Corresponding Authors

*E-mail: satya504@gmail.com.
*E-mail: rkatiyar@hpcf.uprrp.edu.

Notes

The authors declare no competing financial interest.

■ ACKNOWLEDGMENTS

The authors acknowledge financial support from DOE (Grant DE-FG02-R46526). S.S. thanks NSF (EPS-01002410) for fellowship. We thank Majid Ahmadi and Prof. Maxime J.-F. Guinel for their help in the TEM and EELS measurements. J.-W.J. acknowledges support of the Recruitment Program of Global Youth Experts of China and the start-up funding from Shanghai University.

■ REFERENCES

(1) Juutilainen, A.; Ahlskog, M.; Volodin, A. Measurements of Tunneling Conduction to Carbon Nanotubes and Its Sensitivity to Oxygen Gas. *Phys. Rev. B* **2012**, *86*, 17−27.

(2) Delgado, J. L.; Herranz, M.; Martin, N. The Nano-Forms of Carbon. *J. Mater. Chem.* **2008**, *18*, 1417.

(3) Iijima, S. Helical Microtubules of Graphitic Carbon. *Nature* **1991**, *354*, 56−58.

(4) Slifka, A. J.; Singh, G.; Lauria, D. S.; Rice, P.; Mahajan, R. L. Observations of Nanobubble Formation on Carbon Nanotubes. *Appl. Phys. Express* **2010**, *3*, 065103−3.

(5) Dresselhaus, M. S.; Dresselhaus, G.; Saito, R. Physics of Carbon Nanotubes. *Carbon* **1995**, *33*, 883−91.

(6) Balandin, A. A. Thermal Properties of Graphene and Nanostructured Carbon Materials. *Nat. Mater.* **2011**, *10*, 569−581.

(7) Avouris, P. Molecular Electronics with Carbon Nanotubes. *Acc. Chem. Res.* **2002**, *35*, 1026−1034.

(8) Guldi, D. M.; Rahman, G. M. A.; Zerbetto, F.; Maurizio, P. Carbon Nanotubes in Electron Donor-Acceptor Nanocomposites. *ChemInform* **2006**, *37*, 871−878.

(9) Bai, Y.; Huang, Z. H.; Kang, F. Synthesis of Reduced Graphene Oxide/Phenolic Resin-based Carbon Composite Ultrafine Fibers and Their Adsorption Performance for Volatile Organic Compounds and Water. *J. Mater. Chem. A* **2013**, *1*, 9536.

(10) Pop, E.; Mann, D. A.; Goodson, K. E.; Dai, H. Electrical and Thermal Transport in Metallic Single-Wall Carbon Nanotubes on Insulating Substrates. *J. Appl. Phys.* **2007**, *101*, 093710.

(11) Panzer, M. A.; Duong, H. M.; Okawa, J.; Shiomi, J.; Wardle, B. L.; Maruyama, S.; Goodson, K. E. Temperature-Dependent Phonon Conduction and Nanotube Engagement in Metalized Single Wall Carbon Nanotube Films. *Nano Lett.* **2010**, *10*, 2395−2400.

(12) Behnam, A.; Hersam, M. C.; Pop, E.; Marks, T. J.; Lauhon, L. J.; Hoag, A. J.; Jariwala, D.; Estrada, D.; Lian, F.; Zhong, X.; Sangwan, V. K. High-Field Transport and Thermal Reliability of Sorted Carbon Nanotube Network Devices. *ACS Nano* **2013**, *7*, 482−490.

(13) Pop, E.; Mann, D.; Wang, Q.; Goodson, K.; Dai, H. Thermal Conductance of an Individual Single-Wall Carbon Nanotube above Room Temperature. *Nano Lett.* **2006**, *6*, 96−100.

(14) Marconnet, A. M.; Panzer, M. A.; Goodson, K. E. Thermal Conduction Phenomena in Carbon Nanotubes and Related Nanostructured Materials. *Rev. Mod. Phys.* **2013**, *85*, 1295−1326.

(15) Kim, D.; Zhu, L.; Han, C. S.; Kim, J. H.; Baik, S. Raman Characterization of Thermal Conduction in Transparent Carbon Nanotube Films. *Langmuir* **2011**, *27*, 14532−14538.

(16) Ruoff, R. Mechanical And Thermal Properties of Carbon Nanotubes. *Carbon* **1995**, *33*, 925−930.
(17) Marconnet, A. M.; Yamamoto, N.; Panzer, M. A.; Wardle, B. L.; Goodson, K. E. Thermal Conduction in Aligned Carbon Nanotube−Polymer Nanocomposites with High Packing Density. *ACS Nano* **2011**, *5*, 4818−4825.
(18) Yu, C.; Choi, K.; Yin, L.; Grunlan, J. C. Light-Weight Flexible Carbon Nanotube Based Organic Composites with Large Thermoelectric Power Factors. *ACS Nano* **2011**, *5*, 7885−7892.
(19) Callister, W. D.; Rethwisch, D. G. *Fundamentals of Materials Science and Engineering: An Integrated Approach*, 3rd ed.; John Wiley & Sons: Hoboken, NJ, 2008.
(20) Sahoo, S.; Arora, A. K. Laser Power Induced Multiphonon Resonant Raman Scattering in CdS Nanoparticles. *J. Phys. Chem. B* **2010**, *114*, 4199−4203.
(21) Dresselhaus, M. S.; Dresselhaus, G.; Saito, R.; Jorio, A. Raman Spectroscopy of Carbon Nanotubes. *Phys. Rep.* **2005**, *409*, 47−99.
(22) Khlobystov, A. N. Carbon Nanotubes: From Nano Test Tube to Nano-Reactor. *ACS Nano* **2011**, *5*, 9306−9312.
(23) Sreeprasad, T. S.; Nguyen, P.; Kim, N.; Berry, V. Controlled, Defect-Guided, Metal-Nanoparticle Incorporation onto MoS_2 via Chemical and Microwave Routes: Electrical, Thermal, and Structural Properties. *Nano Lett.* **2013**, *13*, 4434−4441.
(24) Zhu, H.; Li, Y.; Fang, Z.; Xu, J.; Cao, F.; Wan, J.; Preston; Yang, C. B.; Hu, L. Highly Thermally Conductive Papers with Percolative Layered Boron Nitride Nanosheets. *ACS Nano* **2014**, *8*, 3606−3613.
(25) Ago, H.; Imamura, S.; Okazaki, T.; Saito, T.; Yumura, M.; Tsuji, M. CVD Growth of Single-Walled Carbon Nanotubes with Narrow Diameter Distribution over Fe/MgO Catalyst and Their Fluorescence Spectroscopy. *J. Phys. Chem. B* **2005**, *109*, 10035−10041.
(26) Lammps. http://www.cs.sandia.gov/~sjplimp/lammps.html (2012).
(27) Stuart, S. J.; Tutein, A. B.; Harrison, J. A. A Reactive Potential for Hydrocarbons with Intermolecular Interactions. *J. Chem. Phys.* **2000**, *112*, 6472.
(28) Ikeshoji, T.; Hafskjold, B. Non-Equilibrium Molecular Dynamics Calculation of Heat Conduction in Liquid and through Liquid-Gas Interface. *Mol. Phys.* **1994**, *81*, 251−261.
(29) Jiang, J.-W.; Park, H. S.; Rabczuk, T. Molecular Dynamics Simulations of Single-Layer Molybdenum Disulphide (MoS_2): Stillinger-Weber Parametrization, Mechanical Properties, and Thermal Conductivity. *J. Appl. Phys.* **2013**, *114*, 064307.
(30) Pimenta, M.; Dresselhaus, G.; Smalley, R.; Eklund, P.; Rao, A.; Hanlon, E.; Bawendi, M.; Empedocles, S.; Marucci, A.; Dresselhaus, M. Raman Modes of Metallic Carbon Nanotubes. *Phys. Rev. B* **1998**, *58*, R16016−R16019.
(31) Fantini, C.; Jorio, A.; Souza, M.; Strano, M.; Dresselhaus, M.; Pimenta, M. Optical Transition Energies for Carbon Nanotubes from Resonant Raman Spectroscopy: Environment and Temperature Effects. *Phys. Rev. Lett.* **2004**, *93*, 147406.
(32) Naumov, A. V.; Ghosh, S.; Tsyboulski, D. A.; Bachilo, S. M.; Weisman, R. B. Analyzing Absorption Backgrounds in Single-Walled Carbon Nanotube Spectra. *ACS Nano* **2011**, *5*, 1639−1648.
(33) Li, H. D.; Zhang, Y.; Zou, G. T.; Yang, H. B.; Yang, R. S.; Liu, B. B.; Gu, Z. N.; Shi, Z. J.; Zhang, S. L.; Zhou, L. X.; Zhan, Y.; Lian, Z. L.; Yue, K. T.; Iijima, S. Temperature Dependence of the Raman Spectra of Single-Wall Carbon Nanotubes. *Appl. Phys. Lett.* **2000**, *76*, 2053.
(34) Daniel, K.; Lu, J. Vibrational Modes of Carbon Nanotubes and Nanoropes. *Phys. Rev. B* **1999**, *60*, 6535−6540.
(35) Uchida, T.; Tazawa, M.; Sakai, H.; Yamazaki, A.; Kobayashi, Y. Radial Breathing Modes of Single-Walled Carbon Nanotubes in Resonance Raman Spectra at High Temperature and Their Chiral Index Assignment. *Appl. Surf. Sci.* **2008**, *254*, 7591−7595.
(36) Popov, V. Carbon Nanotubes: Properties and Application. *Mater. Sci. Eng., R* **2004**, *43*, 61−102.
(37) Rao, A. M. Diameter-Selective Raman Scattering from Vibrational Modes in Carbon Nanotubes. *Science* **1997**, *275*, 187−191.
(38) Pimenta, M. A.; Marucci, A.; Brown, S. D. M.; Matthews, M. J.; Rao, A. M.; Eklund, P. C.; Smalley, R. E.; Dresselhaus, G. Resonant Raman effect in Single-Wall Carbon Nanotubes. *J. Mater. Res.* **1998**, *13*, 2405−2411.
(39) Saito, R.; Hofmann, M.; Dresselhaus, G.; Jorio, A.; Dresselhaus, M. S. Raman Spectroscopy of Graphene and Carbon Nanotubes. *Adv. Phys.* **2011**, *60*, 413−550.
(40) Jorio, A.; Liu, C.; Saito, R.; Rao, A.; Pimenta, M.; Dantas, M.; Souza, M.; Dresselhaus, M.; Dresselhaus, G.; Cheng, H. Polarized Raman Study of Single-Wall Semiconducting Carbon Nanotubes. *Phys. Rev. Lett.* **2000**, *85*, 2617−2620.
(41) Saito, R.; Takeya, T.; Kimura, T.; Dresselhaus, G.; Dresselhaus, M. Raman Intensity of Single-Wall Carbon Nanotubes. *Phys. Rev. B* **1998**, *57*, 4145−4153.
(42) Sahoo, S.; Gaur, A. P. S.; Ahmadi, M.; Guinel, M. J.-F.; Katiyar, R. S. Temperature-Dependent Raman Studies and Thermal Conductivity of Few-Layer MoS_2. *J. Phys. Chem. C* **2013**, *117*, 9042−9047.
(43) Lee, J. U.; Yoon, D.; Kim, H.; Lee, W. S.; Cheong, H. Thermal Conductivity of Suspended Pristine Graphene Measured by Raman Spectroscopy. *Phys. Rev. B* **2011**, *83*, 081419−4.
(44) Calizo, I.; Balandin, A. A.; Bao, W.; Miao, F.; Lau, C. N. Temperature Dependence of the Raman Spectra of Graphene and Graphene Multilayers. *Nano Lett.* **2007**, *7*, 2645−2649.
(45) Peercy, P. S.; Morosin, B. Pressure and Temperature Dependences of the Raman-Active Phonons in SnO_2. *Phys. Rev. B* **1973**, *7*, 2779−2786.
(46) Ridley, B. K. *Electrons and Phonons in Semiconductor Multilayers*; Cambridge University Press: Cambridge, U.K., 1997.
(47) Menéndez, J.; Cardona, M. Temperature Dependence of the First-Order Raman Scattering by Phonons in Si, Ge, and α-Sn: Anharmonic Effects. *Phys. Rev. B* **1984**, *29*, 2051.
(48) Jorio, A.; Filho, A. G. S; Brar, V. W.; Swan, A. K.; Unlu, M. S.; Goldberg, B. B.; Righi, A.; Hafner, J. H.; Lieber, C. M.; Saito, R.; Dresselhaus, G.; Dresselhaus, M. S. Polarized Resonant Raman Study of Isolated Single-Wall Carbon Nanotubes: Symmetry Selection Rules, Dipolar and Multipolar Antenna Effects. *Phys. Rev. B* **2002**, *65*, 121402.
(49) Tritt, T. M. *Thermal Conductivity: Theory, Properties, and Applications*; Kluwer Academic/Plenum Publishers: New York, 2004.
(50) Balandin, A. A.; Ghosh, S.; Bao, W.; Calizo, I.; Teweldebrhan, D.; Miao, F.; Lau, C. N. Superior Thermal Conductivity of Single-Layer Graphene. *Nano Lett.* **2008**, *8*, 902−907.
(51) Egerton, R. F.; Cheng, S. C. Measurement of Local Thickness by Electron Energy-Loss Spectroscopy. *Ultramicroscopy* **1987**, *21*, 231−244.
(52) Kim, P.; Shi, L.; Majumdar, A.; Mc Euen, P. L. Thermal Transport Measurement of Individual Multiwalled Nanotubes. *Phys. Rev. Lett.* **2001**, *87*, 215502−4.
(53) Vollebregt, S.; Banerjee, S.; Beenakker, K.; Ishihara, R. Thermal Conductivity of Low Temperature Grown Vertical Carbon Nanotube Bundles Measured using the Three-ω Method. *Appl. Phys. Lett.* **2013**, *102*, 191909.
(54) Jiang, J.-W.; Wang, J.-S. Theoretical Study of Thermal Conductivity in Single-Walled Boron Nitride Nanotubes. *Phys. Rev. B* **2011**, *84*, 085439.